# Greenland ice velocity maps from the PROMICE project

Anne Solgaard[1], Anders Kusk[2], John Peter Merryman Boncori[2], Jørgen Dall[2], Kenneth D. Mankoff[1],
Andreas P. Ahlstrøm[1], Signe B. Andersen[1], Michele Citterio[1], Nanna B. Karlsson[1], Kristian
K. Kjeldsen[1], Niels J. Korsgaard[1], Signe H. Larsen[1], and Robert S. Fausto[1]

[1]The Geological Survey of Denmark and Greenland, Østervoldgade 10, 1350 København K, Danmark
[2]Technical University of Denmark - National Space Institute, Ørsteds Plads 348, 2800 Kongens Lyngby, Denmark

**Correspondence:** Anne Solgaard (aso@geus.dk)

**Abstract.** We present the Programme for Monitoring of the Greenland Ice Sheet (PROMICE) ice velocity product
(https://doi.org/10.22008/promice/data/sentinel1icevelocity/greenlandicesheet (Solgaard and Kusk, 2021)) which is a September 2016 through present time series of Greenland Ice Sheet ice velocity mosaics. The product is based on Sentinel-1 synthetic aperture radar data and has a 500 m spatial resolution. A new mosaic is available every 12 days and span two consecutive
5    Sentinel-1 cycles (24 days). The product is made available within ∼10 days of the last acquisition and includes all possible 6 and 12 day pairs within the two Sentinel-1A cycles. We describe our operational processing chain in high detail from data selection, mosaicking and error estimation to final outlier removal. The product is validated against in-situ GPS measurements. We find that the standard deviation of the difference between satellite and GPS derived velocities is 20 m/yr and 27 m/yr for the $v_x$ and $v_y$ components, respectively. This is within the expected bounds, however, we expect that the GPS measurements
10   carry a considerable part of this uncertainty. We investigate variations in coverage from both a temporal and spatial perspective. Best spatial coverage is achieved in winter due to excellent data coverage and high coherence, while summer mosaics have the lowest coverage due to widespread melt. The southeast Greenland Ice Sheet margin, along with other areas of high accumulation and melt, often have gaps in the ice velocity mosaics. The spatial comprehensiveness and temporal consistency make the product ideal for monitoring and studying ice-sheet wide ice discharge and dynamics of glaciers.

15  ## 1   Introduction

The Greenland Ice Sheet (GrIS) is a major contributor to sea-level rise, and approximately half of this contribution is due to ice dynamics (Shepherd et al., 2019; Mankoff et al., 2020). Thus, in order to constrain the on-going mass loss of the Greenland Ice Sheet it is important to obtain observations of ice-flow velocities. High temporal and spatial resolution will further allow us to distinguish between annual or sub-annual variations and long-term trends, aiding in improving our understanding of the
20   processes behind the observed changes. This is especially important because the flow of glaciers and ice caps vary on a range of timescales in response to the seasonal cycles, climate change, or internal variability (e.g. Moon et al., 2020; Joughin et al., 2018; Mouginot et al., 2018). In-situ measurements of ice-flow velocities are relatively sparse on the GrIS and most of the measurements stem from GPS surveys (Ahlstrøm et al., 2013). The sparseness is due to the inaccessibility of the GrIS and the harsh climatic conditions, which make fieldwork and instrumentation challenging. Satellite observations are thus key for

deriving time series of ice velocity maps, which can increase our understanding of the dynamics of ice and its interactions with the other components of the climate system.

In the past, surface ice-velocity (IV) maps of the Greenland Ice Sheet and its outlet glaciers only resolved annual or seasonal characteristics due to the limited availability of data (e.g. Rignot and Kanagaratnam, 2006; Howat et al., 2010; Moon et al.,
5  2014; Joughin et al., 2010)). This scenario changed with the launch of Landsat 8 (a joint NASA/USGS mission) in 2013, and ESA's Sentinel-1 (2014 and 2016) and Sentinel-2 (2015 and 2017) satellites. With this, freely available data became abundant, especially increasing the temporal resolution and spatial coverage of ice-velocity products. At present, several freely available GrIS wide velocity products exist with different temporal resolution e.g. annual, quarterly and monthly mosaics from Copernicus Climate Change Service, ESA-CCI (Nagler et al., 2015) and NASA's MEaSUREs program (e.g. Joughin, 2020a,
10  c, b) including the ITS_LIVE project (Gardner et al., 2019) based on SAR and/or optical data. These are updated periodically with a lag. Scene pair velocities over Greenland from Landsat are available from NASA MEaSUREs ITS_LIVE at present up until 2018 (Gardner et al., 2019) and from TU Dresden covering the period (1972–2015) (Rosenau et al., 2015). Furthermore, Mouginot et al. (2019a, b, c, d) provide a freely available product comprising annual ice velocity mosaics for the GrIS spanning the period 1972 to 2017 based on both optical and SAR data.

15  Here we present the Programme for the Monitoring of the Greenland Ice Sheet (PROMICE) (www.promice.org) ice velocity product, which is a time series of ice velocity mosaics based on Sentinel-1 SAR offset-tracking. This work is part of the PROMICE monitoring effort focusing on the GrIS. The product benefits from the abundance, continuity, and high temporal resolution of the Sentinel-1 SAR data, and is continuously updated every 12 days. The product is used as input to, for example, the solid ice discharge product by Mankoff et al. (2020) and to study GrIS wide glacier dynamics in high temporal detail in
20  Vijay et al. (2019). In the following sections we describe the IV product, the data it is derived from, the operational setup, and the data processing steps that are used to generate it. Finally, we make use of available GPS measurements in order to validate our velocity product.

## 2  The PROMICE ice velocity Product

The PROMICE ice velocity product (https://doi.org/10.22008/promice/data/sentinel1icevelocity/greenlandicesheet (Solgaard
25  and Kusk, 2021)) is a geospatial time series of Greenland wide ice velocity mosaics produced using the IPP processor (see Section 4). The product spans the period September 13 2016 to present and has a spatial resolution of 500 m and a temporal resolution of 24 days. The product is based on measurements of displacements between pairs of radar images acquired 6 or 12 days apart (see Section 3.1). To achieve a consistent coverage (see Section 6), each mosaic is a weighted average of velocity measurements from all possible 6 and 12 day pairs using data from Sentinel-1A and 1B within two consecutive Sentinel-1A
30  orbit cycles (i.e.24 days). A given mosaic thus overlaps by 12 days with the previous and subsequent maps. A new map is produced for every Sentinel-1A cycle i.e. a new mosaic every 12 days. We aim to provide a new mosaic within 10 days of the last acquisition. The velocity provided at every grid point in the PROMICE ice velocity product is the weighted average of all velocity measurements available at that grid point within that 24-day period (see Section 4.4), and should be considered
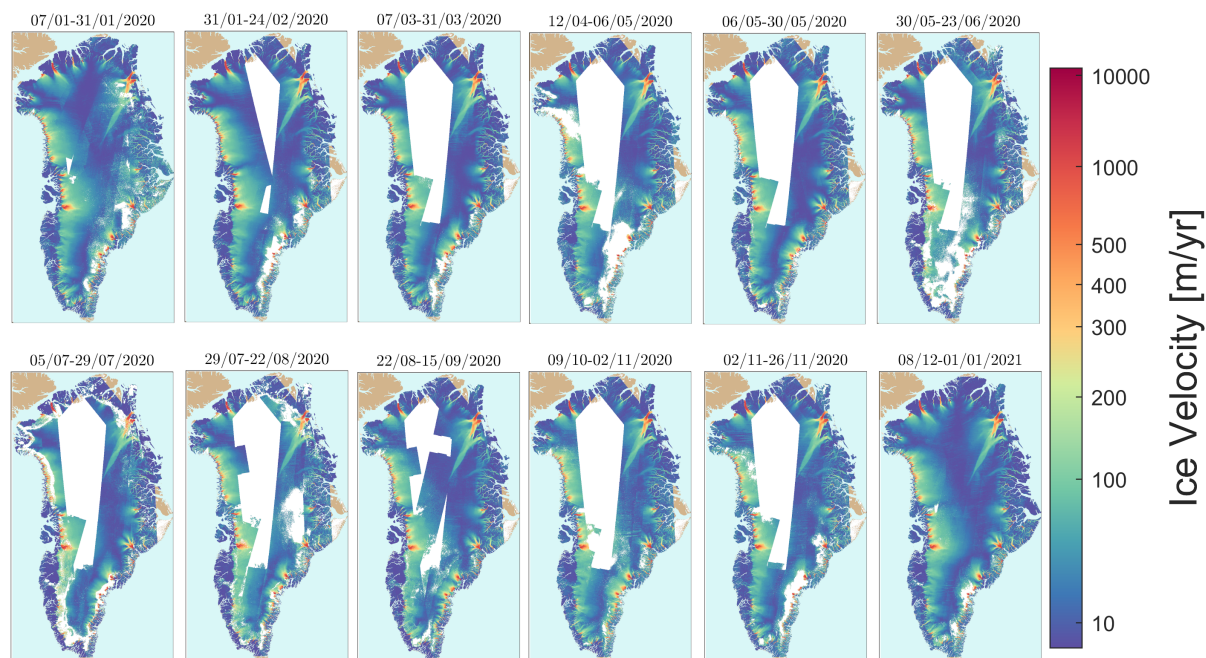
**Figure 1.** Examples of the PROMICE ice velocity maps: From top left corner to lower right approximately one map per month over 2020.

an average estimate of velocity over the 24-day period during which the radar images were acquired (see further discussion in Section 6). The start and end times of this period are given in the *time_bnds* variable in the PROMICE NetCDF product (see below). Figure 1 shows samples of the timeseries at different times during the year.

Each IV mosaic is supplied as a single NetCDF file following the Climate Forecast (CF) conventions (see https://cfconventions.org/). The mosaics are provided on a 500 m Polar Stereographic Greenland-wide grid with latitude of true scale at 70°N and reference longitude -45°E (EPSG 3413 projection). The variables in the NetCDF product are listed in Table 1. A quick look image for each mosaic is provided along with the dataset.

## 3   Data

In the following, we present the characteristics of the Sentinel-1 data and introduce the input data that we use to generate the PROMICE ice velocity product.

### 3.1   Sentinel-1 SAR Data Characteristics

SAR sensors are well suited for polar observations because data collection is not impacted by the polar night or cloud cover. The Sentinel-1 constellation currently consists of two satellites, Sentinel-1A and Sentinel-1B, equipped with identical C-band (5.4 GHz) SAR sensors. Over the GrIS, the Sentinel-1 SAR mainly employs the Interferometric Wideswath (IW) mode (De

**Table 1.** Variables in the PROMICE ice velocity NetCDF product

| Variable | Description | Unit |
|---|---|---|
| x | x-coordinate of projection | m |
| y | y-coordinate of projection | m |
| time | Midpoint time of all contributing acquisitions | Days since 1990-1-1 |
| time_bnds | First and last time of contributing acquisitions | Days since 1990-1-1 |
| land_ice_surface_easting_velocity | Ice velocity along x-axis | m/d |
| land_ice_surface_northing_velocity | Ice velocity along y-axis | m/d |
| land_ice_surface_vertical_velocity | Vertical velocity from surface parallel flow | m/d |
| land_ice_surface_velocity_magnitude | Horizontal ice velocity magnitude | m/d |
| land_ice_surface_easting_velocity_std | Ice velocity error estimate along x-axis | m/d |
| land_ice_surface_northing_velocity_std | Ice velocity error estimate along y-axis | m/d |
| land_ice_surface_velocity_magnitude_std | Horizontal ice velocity error estimate | m/d |

Zan and Guarnieri, 2006) allowing for generation of radar images with a resolution of approximately 3 m on ground in the slant range (line-of-sight direction) and 22 m in the azimuth (flight-path direction). The near-polar orbit has a repeat cycle of 175 orbits, corresponding to 12 days, with the two satellite orbits phased 6 days apart. With the current observation schedule, the entire margin of Greenland is imaged every 12 days by both satellites (Fig. 2A). Furthermore, the entire ice sheet is mapped from several additional tracks every winter from December to February, allowing the generation of Greenland-wide maps during this season (Fig. 2B).

SAR-based ice-velocity measurements are based on processing of image pairs. Images acquired within short time intervals (temporal baselines) retain a high degree of coherence (see Section 5.3) and therefore measurement coverage, however they also exhibit an increased sensitivity to error sources, which do not depend on the temporal baseline (e.g. processing artifacts, ionospheric and orbit estimation errors, see 5).

Image pairs can be formed between acquisitions from the same satellite, i.e. S1A-S1A or S1B-S1B, with temporal baselines which are a multiple of 12 days, i.e. 12-days, 24-days etc. In addition, image pairs can also be formed from acquisitions obtained from two different satellites, i.e. S1A-S1B or S1B-S1A, with a temporal baseline which is an odd multiple of 6-days, i.e. 6-days, 18-days, etc. Although in principle the radar instruments on board the Sentinel-1A and -1B satellites are identical, there are some subtle differences, which should be taken into account when selecting the data pairs for processing, as detailed in sections 4.1 and 5.2.

### 3.2 Input Data

The data used for generating the PROMICE ice velocity product are single-look complex (SLC) IW radar images (with annotation), supplied by the Copernicus Open Access Hub (https://scihub.copernicus.eu/). SLC images are referenced to the radar acquisition geometry and have the highest resolution of the available product types (3 m × 22 m). They are supplied as slices
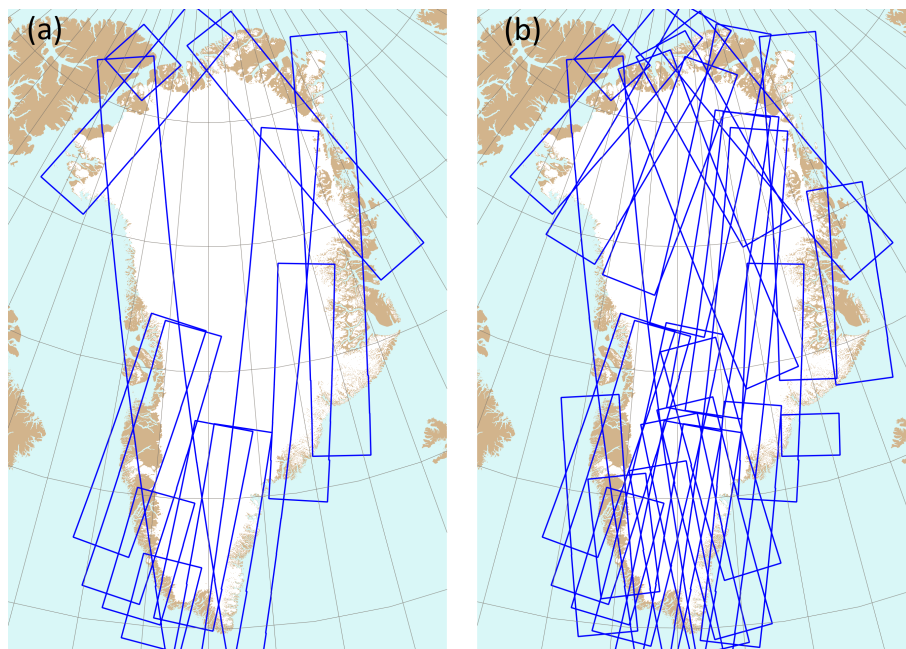
**Figure 2.** Typical Sentinel-1 coverage over Greenland for a single 12-day orbital cycle, (a) during the normal observation scenario, (b) during the dedicated winter campaign. The blue polygons represent radar images from different tracks, acquired at different times during the cycle.

with a footprint of approximately 250 km×250 km. Owing to the peculiarities of the IW mode, each slice is subdivided into three range swaths, named IW1-IW3, which are acquired in an interleaved (bursted) fashion; these swaths are stored in separate files. The SLC images are supplemented by restituted orbit files, available a few hours after acquisition, and precise orbit files, available 21 days after the data acquisition at http://aux.sentinel1.eo.esa.int/POEORB/. Since the PROMICE ice velocity product is typically generated before the latter become available, we use the restituted orbit files as we have found that the difference between the restituted orbit files and the precice orbit files is insignificant for our data products (see Section 5.1).

In order to geocode measurements made in radar geometry, a digital elevation model (DEM) is used. We employ the GIMP DEM (Howat et al., 2014), downsampled to 500 m spacing to match the resolution of the IV product.

## 4   Methods

The data processing is carried out using the IPP processor, a highly automated processing chain requiring little user intervention. The processor is developed and maintained by DTU Space (Kusk et al., 2018), and is described in the following sections. An overview of the processing flow can be seen in Fig. 3.
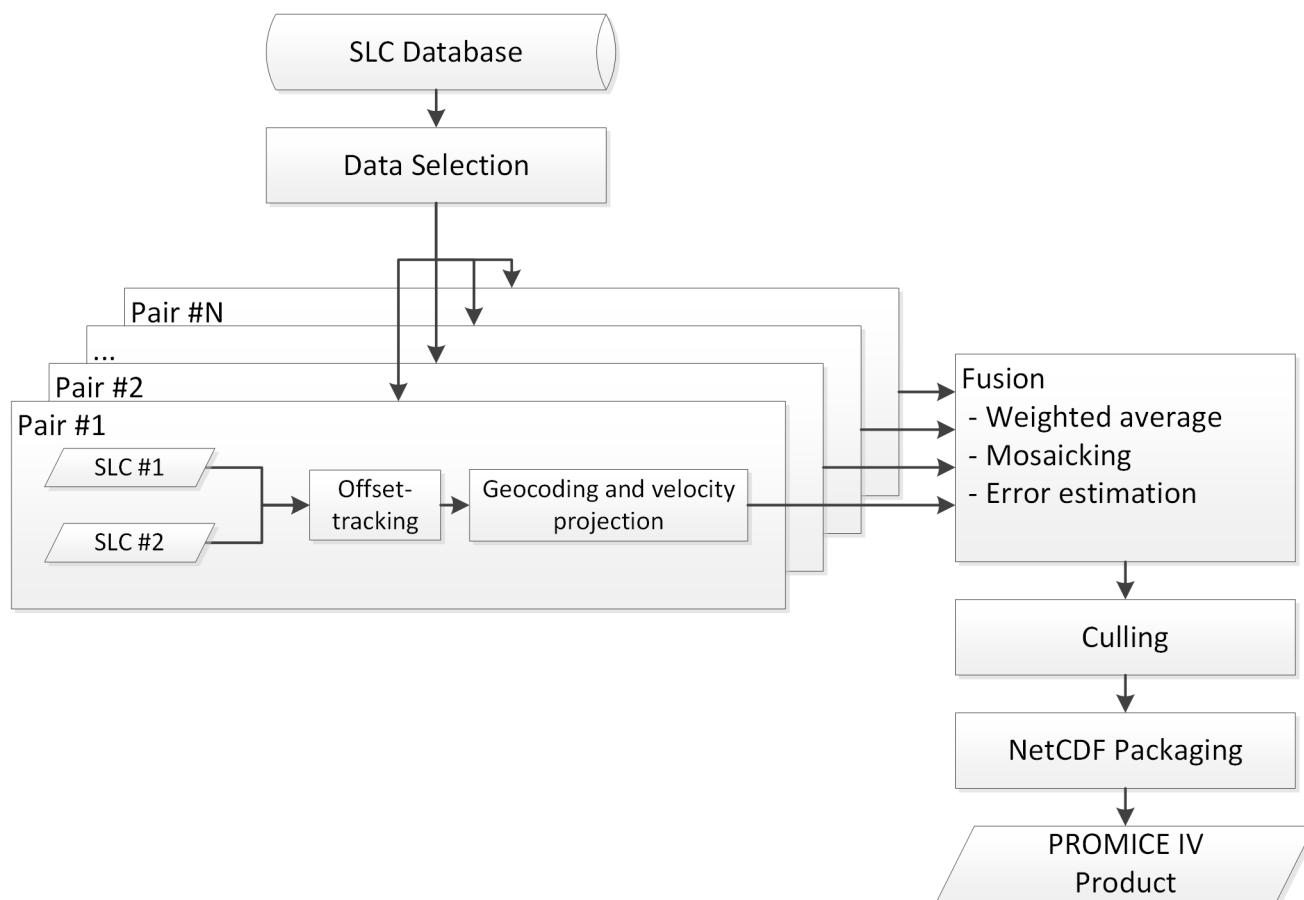
**Figure 3.** Processing flow for PROMICE ice velocity product generation.

## 4.1  Processing Flow

To support the PROMICE product generation, a database with all available SLC products over Greenland is maintained. This is updated daily by searching the Copernicus Open Access hub. An automated system downloads all new SLC data to a central storage location. Product generation is initiated by an operator selecting a Sentinel-1A reference orbit cycle number. All SLCs from Sentinel-1A in that and the following cycle (24 days of data) are first selected for processing. Additionally, all SLCs from Sentinel-1B acquired within the same 24-day timespan are selected for processing. Then, all possible SLC pairings with a 6- or 12-day baseline are calculated, and the offset-tracking processing described in 4.2 is automatically carried out for each pair. When all pairs required for a product have been processed, the geocoding and error estimation described in 4.3 and 5 is performed for each pair, followed by fusion and mosaicking of all the pairs, as described in 4.4.

## 4.2 Offset-tracking

The offset-tracking procedure employed is similar to the one described in Strozzi et al. (2002) and estimates local shifts between two SLCs in radar geometry. First, the SLC with the earliest acquisition time is used as the reference image. An output grid is defined in the reference image geometry, with a spacing of 40 pixels in the slant-range direction and 10 pixels in the along-

5  track (azimuth) direction. These spacings correspond to approximately 150 m×150 m on the ground. The corresponding points (assuming no motion and including fractions of a pixel) in the second SLC are calculated using the SLC annotation, orbits, and the DEM. Calibration constants in range and azimuth are applied at this stage to correct for the different geolocation biases observed in Sentinel-1A and Sentinel-1B SLCs (see also 5.2). For 12-day pairs, these constants are identical for both SLCs and have no effect.

10  At each grid point, surrounding image patches of 256×64 complex pixels (slant range×azimuth) are extracted in both SLCs. In the second SLC, the patches are extracted at integer pixel locations, with the fractional part saved to be added to the final shift estimate. Each patch is deramped (Miranda, 2017), upsampled by a factor of two (in both range and azimuth) using FFT interpolation, and the intensity (magnitude squared of the complex pixel values) is derived. A normalized cross-correlation of the two upsampled real-valued patches is carried out, resulting in a correlation surface with values between 0 and 1. The

15  integer shift between the two patches is then estimated by locating the peak of the correlation surface, and a 9x9 neighbourhood surrounding the peak is upsampled by a factor of 4. Then the fractional shift is retrieved by fitting a parabola to the peak and its two surrounding pixels in each dimension, correcting finally for oversampling factors and accounting for the fractional shift initially estimated for the second SLC. A signal-to-noise ratio (SNR) for the peak estimate is calculated by dividing the correlation value of the peak with the mean of the surrounding pixels in the correlation surface (de Lange et al., 2007). The

20  estimated 2-D shift, the peak normalized cross correlation value (NCC), and the SNR are all saved for further processing.

The procedure described above will yield a shift estimate even if the two images are completely uncorrelated, so a culling of the estimated shifts is carried out. First, pixels with an NCC<0.05 or SNR<7 are set as invalid. Then, a further culling, based on local medians in a 5×5 neighbourhood, is carried out using the procedure described in Westerweel and Scarano (2005). These steps will remove most outliers, but some may remain, especially in areas subject to surface melt, as the associated strong radar

25  backscatter can create false correlation peaks. An additional culling based on timeseries statistics (see Section 4.4) is carried out on the final mosaicked product to further suppress these outliers.

To aid in error estimation, the local standard deviations of the two shift maps (range and azimuth shifts) are estimated in a sliding 5×5 window, ignoring pixels with invalid measurements, and the shift maps are finally averaged by a 5×5 window. The shift maps (in units of SLC pixels) and associated standard deviations are stored along with the SLC parameters and orbit

30  information to be used in the subsequent processing.

## 4.3 Geocoding and horizontal velocity projection

The geocoding takes as input the shift maps and associated standard deviation maps output by the offset-tracking and the DEM. Using the DEM and orbit information, the maps are resampled to the output grid in map projection (see Section 2). The shifts

and standard deviations are converted to velocity by multiplying with the SLC pixel spacing and dividing by the temporal baseline. At this stage, the velocities and standard deviations, even though provided on a georeferenced grid, are still measured in the radar range/azimuth geometry. With a single pair providing only two velocity measurements, it is not directly possible to estimate three-dimensional flow. Instead, we assume surface parallel flow (SPF) and estimate the flow as described in the

5    following. Let $\mathbf{v}_{xyz} = [v_x, v_y, v_z]^T$ be the three-dimensional velocity vector in map geometry, and $\mathbf{v}_{SAR} = [v_r, v_a]^T$ be the velocity vector in radar geometry, with $v_r$ the range (line-of-sight) velocity and $v_a$ the azimuth (along-track) velocity. With the SPF assumption, the vertical velocity component becomes (Joughin et al., 1998):

$$v_z = (\frac{\partial z}{\partial x} v_x + \frac{\partial z}{\partial y} v_y) \tag{1}$$

The partial derivatives can be derived from the DEM, and the relation between the horizontal and the radar velocity can be
10   written as:

$$\begin{bmatrix} v_r \\ v_a \end{bmatrix} = \begin{bmatrix} \cos\theta\cos\phi + \sin\theta\frac{\partial z}{\partial x} & \cos\theta\sin\phi + \sin\theta\frac{\partial z}{\partial y} \\ -\sin\phi & \cos\phi \end{bmatrix} \begin{bmatrix} v_x \\ v_y \end{bmatrix} \tag{2}$$

where angles $\phi$ and $\theta$ describe the orientation of the line-of-sight (LoS) vector pointing from the pixel under consideration to the sensor, with the horizontal angle $\phi$ measured counter-clockwise from the $y$-axis of the map projection and the elevation angle $\theta$ measured from the local horizontal plane to the LoS vector. The horizontal velocity components (and the associated
15   standard deviation maps) can then be found by inversion of Eq. 2. Projection scaling factors are not applied to the velocities, so these represent physical velocities along the projection axes.

### 4.4   Fusion

The fusion step describes the process of combining and mosaicking the geocoded offset-tracking results on to a Greenland-wide grid. For every pixel on the output grid, we do a weighted averaging of the $N$ valid velocity measurements from all pairs
20   covering the pixel, using as weights the inverse of the measurement variances:

$$\hat{v} = \sum_{n=1}^{N} \frac{1}{\sigma_n^2} v_n \cdot (\sum_{n=1}^{N} \frac{1}{\sigma_n^2})^{-1} \tag{3}$$

where $\hat{v}$ is the fused ($x$ or $y$) velocity, $v_n$ is the ($x$ or $y$) velocity measurement from pair $n$, and $\sigma_n$ its associated standard deviation. The estimated standard deviation of the pixel is then:

$$\hat{\sigma} = \sqrt{(\sum_{n=1}^{N} \frac{1}{\sigma_n^2})^{-1}} \tag{4}$$

25   ### 4.5   Culling

After all measurements have been fused and mosaicked, temporal culling is carried out to remove further outliers. This relies on comparison of the measured value with an average value of all available measurements, based at the time of writing on more

than 4 years of data. For each pixel, we reject the measurement, if:

$$\frac{\sqrt{(\hat{v}_x - v_{m,x})^2 + (\hat{v}_y - v_{m,y})^2}}{\sqrt{v_{m,x}^2 + v_{m,y}^2} + v_\epsilon} > k_{thr} \tag{5}$$

where $(\hat{v}_x, \hat{v}_y)$ is the fused velocity measurement, $(v_{m,x}, v_{m,y})$ is the average velocity, $v_\epsilon$ is a velocity constant preventing erroneous culling in areas with very low velocities, and $k_{thr}$ is a constant factor, setting the threshold for culling. A low value of $k_{thr}$ will remove more outliers, but may also remove valid measurements in areas with strong seasonal variation, such as glaciers with significant speed up during the melt season. This effect is showcased for ice velocity along the flowline from Hagen Bræ in North Greenland (Fig. 4a). The slow flowing outlet glacier in North Greenland experiences periods of speed up during summer, where velocities near the terminus increases more than 200%. At the same time surface melt inhibits processing parts of the data resulting in spikes in the ice velocity as evident in Fig. 4b. Figure 4c and d show how values of $k_{thr}$=3 and 1 cull the data. For $k_{thr}$=3, the (real) summer speed up near the front is conserved, while the majority of spikes further inland are removed. Applying a stricter value, $k_{thr}$=1 removes not only outliers but also the real signal due to summer speed-up. For the PROMICE ice velocity product we apply, $v_\epsilon = 20$ m/yr, whereas $k_{thr} = 3$. This choice of threshold is a balance between removing as much noise as possible without removing actual signal in the mosaics encompassing a wide range of ice dynamics.

Figure 5 provides an example of the effect of applying $k_{thr} = 3$ to a map from summer 2018 when surface melt influences the data quality. The unculled and culled maps are displayed in Fig. 5a and b. The location of the culled data points is shown in red in Fig. 5c. Note for example the removal of the noisy areas in the West Greenland ablation zone and locations influenced by ionospheric stripes in the slow moving interior. On average, $\sim 2\,\%$ of the pixels in a mosaic are culled using this procedure. More pixels are culled in summer mosaics than in winter mosaics.

## 5  Error Sources and Estimation

In this section, we describe the error sources affecting the PROMICE ice velocity product in more detail. The error sources can be divided into three main groups:

1. Slowly varying errors, such as those caused by orbit errors (Section 5.1) or other timing biases in the products (Section 5.2).

2. Temporal decorrelation caused by changes in the radar backscatter between observations, see Section 5.3.

3. Ionospheric errors, resulting in localized, but spatially correlated errors in the measured azimuth shift, see Section 5.4.

4. Aliasing errors caused by the need to acquire two observations from which we infer displacement, and then velocity. Any extreme velocity highs or lows will be smoothed out.
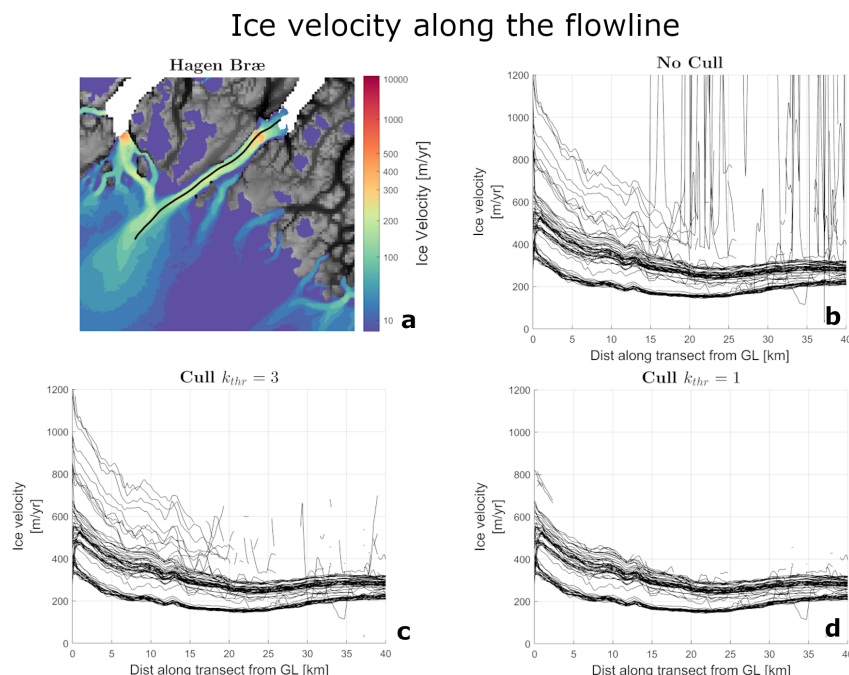
**Figure 4.** The effect of the culling procedure: Example from Hagen Bræ, North Greenland. The ice velocity along the flowline in a) is plotted for all maps since September 2016 in the case of no culling b), applying $k_{thr}$=3 c) and applying $k_{thr}$=1 d).

## 5.1 Orbit Errors

Errors in the knowledge of the Sentinel-1 satellite orbits will result in an apparent shift between the two SLCs in a pair, translating directly into biases on the velocity measurement. For Sentinel-1 data, absolute orbital errors are on the order of 5cm RMS when using the precise orbit product available after 21 days (Peter et al., 2017). This corresponds to 3 m/yr for a

5  measurement using a 6-day pair and 1.5 m/yr for a 12-day pair. Restituted orbits (which are available shortly after acquisition rather than 21 days later) have a nominal accuracy of 10 cm RMS.

To assess the difference between using restituted and precise orbits, we processed 18 different Sentinel-1 12-day pairs (9 S1A/S1A and 9 S1B/S1B pairs) acquired consecutively over an area in Southwest Greenland where much of the scene in the IW1 swath consists of bedrock. The reason for using only 12-day pairs is to exclude the effect of S1A-S1B biases, which are

10  treated instead in Section 5.2. All pairs were processed twice, using either the precise orbits or the restituted orbits, with all other parameters identical. The processing carried out consisted of offset-tracking and geocoding (see sections 4.2 and 4.3). Averaging for each processed pair the measured range and azimuth velocities over the bedrock area, which can be assumed stationary, gives an estimated average residual velocity error for that pair. The mean of the 18 residual range and azimuth velocity estimates and associated standard deviations are listed in Table 2. We note that the range bias (-0.5 m/yr) and azimuth

15  bias (0.5 m/yr) do not differ between the precise and the restituted orbit files. The range standard deviation is 2.7 m/yr for the
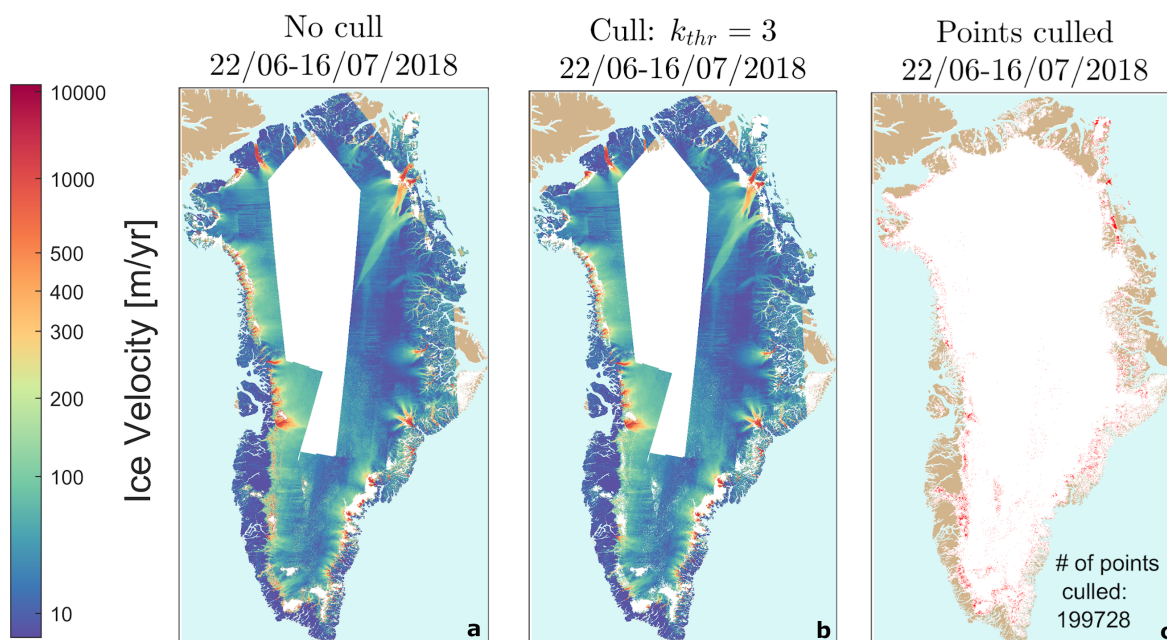
**Figure 5.** The effect of the culling procedure on the Greenland Ice Sheet scale for a map from summer 2018: a)The ice velocity map with no culling applied. b) The same ice velocity map with a culling threshold of $k_{thr}$=3 applied. c) The locations of the culled points are shown as red dots.

**Table 2.** Comparison of precise and restituted orbits files. Range is line of sight and azimuth is along the satellite flight path

| Orbit Type | Range Bias [m/yr] | Range Std [m/yr] | Azimuth Bias [m/yr] | Azimuth Std [m/yr] |
|---|---|---|---|---|
| Precise | -0.5 | 2.7 | 0.4 | 3.3 |
| Restituted | -0.5 | 2.8 | 0.4 | 3.3 |

precise orbit files and 2.8 m/yr for the restituted orbit files, while the azimuth standard deviation is 3.3 m/yr for both orbit types. Overall, the error statistics for the two orbit types are almost completely identical, and the use of restituted versus precise orbits has an insignificant impact on the accuracy of the final velocity products.

**5.2 Geolocation Bias Correction**

5 With the commissioning of Sentinel-1B in late 2016 it became possible to generate ice velocity products with a 6-day temporal baseline by combining Sentinel-1A and Sentinel-1B data (see also 3.2). Although the SAR instruments are in theory identical, our analysis of the initially generated 6-day ice velocity products revealed velocity biases not present in 12-day (same satellite) pairs. To quantify this, an experiment was carried out using 37 Sentinel-1 pairs (9 6-day A/B pairs, 10 6-day B/A pairs, and
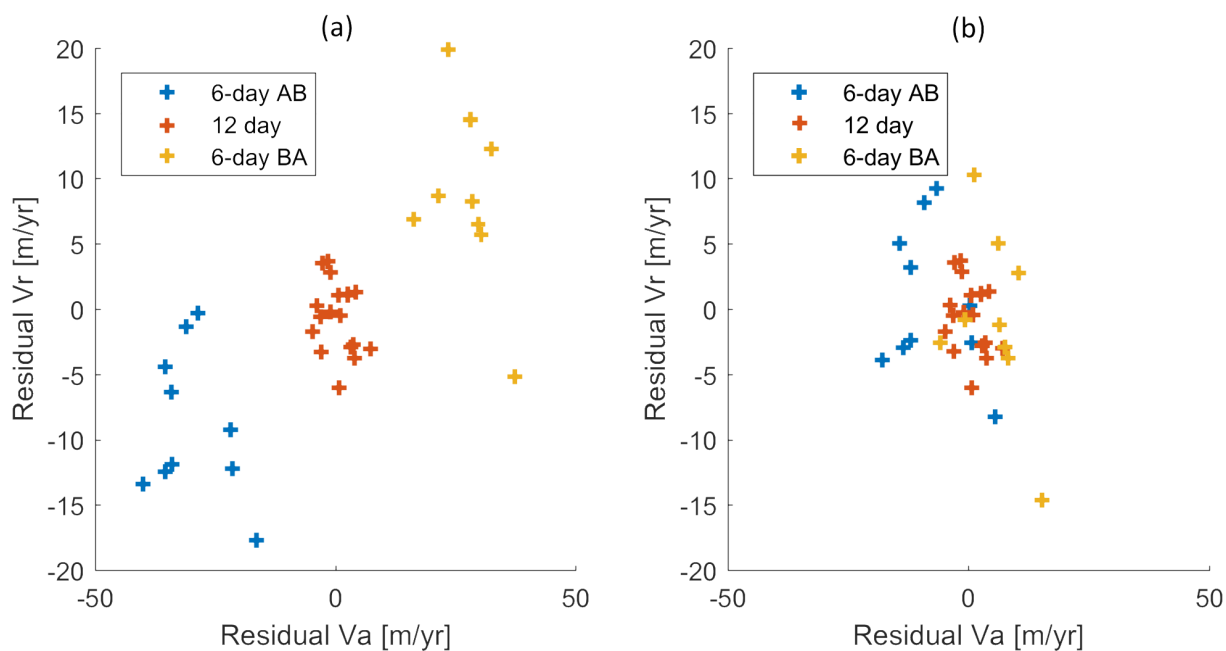
**Figure 6.** Scatterplot of IW1 average residual range and azimuth velocity error of 37 Sentinel-1 pairs, (a) without calibration, (b) calibrated with constants from (Gisinger et al., 2020).

**Table 3.** Velocity biases for different satellite combinations

| Pair Type | Range Bias [m/yr] | Range Std [m/yr] | Azimuth Bias [m/yr] | Azimuth Std [m/yr] |
|---|---|---|---|---|
| 12-day AA/BB | -0.5 | 2.7 | 0.4 | 3.3 |
| Uncalibrated 6-day BA | -8.9 | 5.7 | -29.9 | 7.6 |
| Uncalibrated 6-day AB | 8.6 | 6.9 | 27.5 | 6.3 |
| Calibrated 6-day BA | 0.6 | 5.7 | -7.9 | 7.6 |
| Calibrated 6-day AB | -0.9 | 6.9 | 5.5 | 6.3 |

18 12-day A/A and B/B pairs grouped together). The 18 12-day pairs are identical to the pairs used in 5.1, thus, all pairs were acquired over an area in Southwest Greenland where much of the scene in the IW1 swath consists of bedrock. Averaging the measured range and azimuth velocity over the bedrock area, gives an estimated average residual velocity error for that pair. Figure 6a shows a scatterplot of the residual range velocity ($V_r$) versus residual azimuth velocity ($V_a$) for the 37 pairs. The corresponding mean and standard deviation values are listed in Table 3.

As expected, the 12-day statistics are identical to those observed in the orbit type comparison (see Section 5.1 and Table 2), with a bias magnitude below 0.5 m/yr. For the 6-day pairs (middle part of Table 3), the bias magnitudes are significantly larger

and change sign, depending on whether the first SLC in the pair is acquired from Sentinel-1A or Sentinel-1B. The standard deviations of the 6-day bias estimates are approximately two times those of the 12-day estimates, which is expected, as the velocity measurements are based on measurements of shifts between the images, which are then divided by the temporal baseline to arrive at velocities. The average bias magnitudes for the 6-day pairs are 8.8 m/yr in range and 28.8 m/yr in azimuth.

5   With the 6-day baseline, this corresponds to bias magnitudes on the measured shifts of 0.15 m in range and 0.48 m in azimuth. These values are consistent with results obtained in detailed analysis of Sentinel-1 SLC product geolocation using corner reflectors, see (Schubert et al., 2017) and (Gisinger et al., 2020). The latter reports average shifts between Sentinel-1A and Sentinel-1B of 0.16 m in range and 0.40 m in azimuth, corresponding to velocities of 9.7 m/s and 24.4 m/s, respectively, for measurements using 6-day pairs, but also suggests that there may be a swath dependence of these delays. Our analysis above

10  concerns only the IW1 swath, so for now, we use the constants from (Gisinger et al., 2020) mentioned above to calibrate the PROMICE product. The calibration is implemented as an adjustment to the timing annotation for the SLC products prior to the offset-tracking. Applying these calibration constants to the test dataset described above results in a significantly reduced bias on the 6-day measurements, as shown on Fig. 6b and in the bottom part of Table 3. The calibrated 6-day range velocities now have a mean bias magnitude of 0.8 m/yr, and the azimuth velocities a mean bias of 6.7 m/yr. In the final PROMICE ice

15  velocity product, the weighted averaging of 12-day pairs and both A/B and B/A 6-day pairs will tend to reduce the impact of any residual biases (see also 4.4).

**5.3   Temporal Decorrelation**

Temporal decorrelation is caused by changes in radar backscatter between acquisitions, affecting the ability to measure ice velocity. The surface of the interior of the ice sheet is relatively homogeneous, with no large scale features, and the velocity

20  measurement relies on preservation of the speckle pattern (coherence) between observations (Gray et al., 1998). Speckle is a property of radar images, caused by variations in sub-resolution structure, resulting in large pixel-to-pixel intensity fluctuations in otherwise homogeneous areas. If the scene is moving, but otherwise stable, and the sensor images the scene from the same track, the speckle pattern can be tracked between acquisitions using the cross-correlation procedure described in Section 4.2. Precipitation, surface melt, and rapid ice flow can all reduce the coherence and thus the ability to measure ice velocity in such

25  areas. Often in the interior, the noise level exceeds the signal, but the measurements can still be useful, by averaging multiple measurements to reduce the noise. In extended homogeneous areas of low coherence, the velocity measurements can become noisy and patchy, since many unreliable measurements will be discarded by the culling procedures described in Sections 4.2 and 4.5.

On outlet glaciers, the rapid ice flow and associated deformation tends to destroy the coherence except for short temporal

30  baselines. Here, the ability to measure displacement relies instead on the presence of larger scale features, such as crevasses, which can be still be tracked between images with the cross-correlation procedure described in Section 4.2 even if there is no coherence.

Models that express the shift errors as function of coherence do exist (De Zan, 2014), but the coherence cannot directly be used to estimate errors or discard measurements, since velocity measurements can often still be made in non-coherent, fast
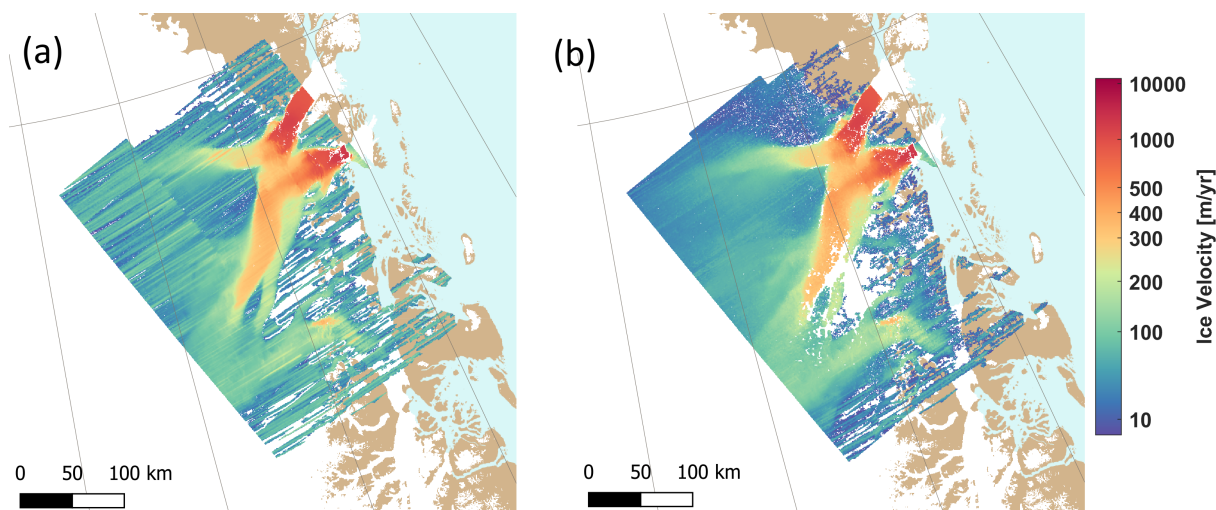
**Figure 7.** Two single-pair velocity maps from relative orbit 74 (ascending), illustrating the impact of ionospheric streaks, (a) 6-day Pair acquired 2016-10-11 and 2016-10-17, with strong ionosphere errors, (b) Pair acquired 2016-10-11 and 2016-10-23, with limited ionosphere errors.

moving areas, as mentioned above. In the PROMICE ice velocity product, the velocity error estimate is based instead on the local standard deviation of the tracked shifts (see Sections 4.2 and 5.5).

## 5.4 Ionospheric Errors

Ionospheric propagation errors arise due to spatial fluctuations (scintillations) in the ionosphere Total Electron Content within the SAR synthetic aperture length (i.e. km-scale variations) (Gray et al., 2000). This is especially a problem in the near-polar regions. For a given image pixel, these fluctuations cause an azimuth variation in the raw signal phase, which is not accounted for by the SAR focusing, resulting in an azimuth shift of the focused pixel. The varying propagation naturally also causes a shift in the range direction, but these shifts are much smaller (typically on the centimeter-level) than those observed in the azimuth direction (comparable to the azimuth pixel size, i.e. several meters (Mattar and Gray, 2002)). The shifts vary along the scene according to the ionosphere conditions along the satellite flight path, often present in only parts of the scene. Also the observed shifts are strongly correlated in the range direction, appearing as linear or slightly curved "streaks" superposed on the azimuth shift map. In the PROMICE velocity mosaics, such streaks are readily identifiable by the human eye, appearing as roughly East-West oriented stripes of varying intensity. The velocity errors caused by ionosphere can exceed 200 m/yr, impacting 6-day pairs twice as much as 12-day pairs, since the shifts caused by the ionopshere do not depend on the temporal baseline. An example of the impact of the ionosphere can be seen in Fig. 7 showing a single-pair 6-day velocity measurement and a 12-day velocity measurement, the former exhibiting significant ionospheric streaks. Both pairs share a common SLC (acquired 2016-10-11), suggesting in this case that the ionosphere effects can be attributed to the other SLC of the 6-day pair.

Methods for reducing the impact of the ionosphere on ice velocity measurements typically rely on the dispersive nature of the ionosphere delay, and have been applied to L-band interferometric ice velocity measurements (Liao et al., 2018). A method for correcting azimuth shift measurements in Sentinel-1 data has been proposed in (Gomba, 2018), but has not been demonstrated for Sentinel-1 ice velocity measurements.

5   The mitigation of ionospheric effects in the PROMICE ice velocity product relies on culling and averaging. Pixels with large ionospheric errors, if present in regions with generally low velocities, will be removed by the temporal culling procedure described in 4.4. In areas where multiple velocity observations are available, the weighted averaging in the fusion (see 4.4) will tend to reduce, but not completely remove, the ionospheric effects. We estimate that the ionospheric effects can cause a velocity error of up to 300 m/yr and will mainly affect the $v_y$-component, which is roughly aligned with the azimuth direction

10  due to the near-polar orbit of the Sentinel-1 satellites.

### 5.5   Error Estimation

The error estimates provided with the PROMICE ice velocity product are derived from the local standard deviation of the underlying shift maps generated by the offset-tracking (see Sections 4.2 and 4.4). As such, they do not account for slowly varying errors, such as those described in Sections 5.1 and 5.2, and only to a limited extent for the impact of ionospheric

15  errors, as these are locally correlated on the scale of the window size used to estimate the local standard deviations. Although this is not a complete error characterization, it was shown in (Boncori et al., 2018) to provide the correct order of magnitude for the errors. Examples of relative error estimates accompanying the two ice velocity maps from Fig. 7 are shown in Fig. 8. The strong ionospheric streaks evident in the 6-day pair on Fig. 7 are seen to be reflected in the corresponding error estimate, although the magnitude is underestimated. In the central and lower left part of the maps, errors are seen to be generally higher

20  on the 12-day pair, but in a more diffuse pattern, even though the 12-day pair is less sensitive to a given shift error, due to the longer baseline. In this case, it is the higher temporal decorrelation of the 12-day pair that causes an increased noise level, which is also reflected in the error estimate.

The slowly varying errors (Sections 5.1 and 5.2) could potentially be corrected by calibrating the measured velocities using ground control points (GCPs), either on stable terrain or in areas where the ice flow is known to vary little. In practice this is

25  difficult to do in an automated system, as the calibration has to be carried out on the individual pairs, where the ionospheric and, to some extent, the temporal decorrelation errors associated with offset-tracking are often much larger than the slowly varying errors. If GCPs are unwittingly selected in areas affected by e.g. ionosphere, the GCP calibration can actually have a detrimental impact. A large number of GCPs, well distributed in the image, would be required to reduce the statistical noise, but this can often not be achieved within the limited spatial coverage of a single pair. For this reason, the PROMICE ice velocity

30  product is not calibrated using GCPs.
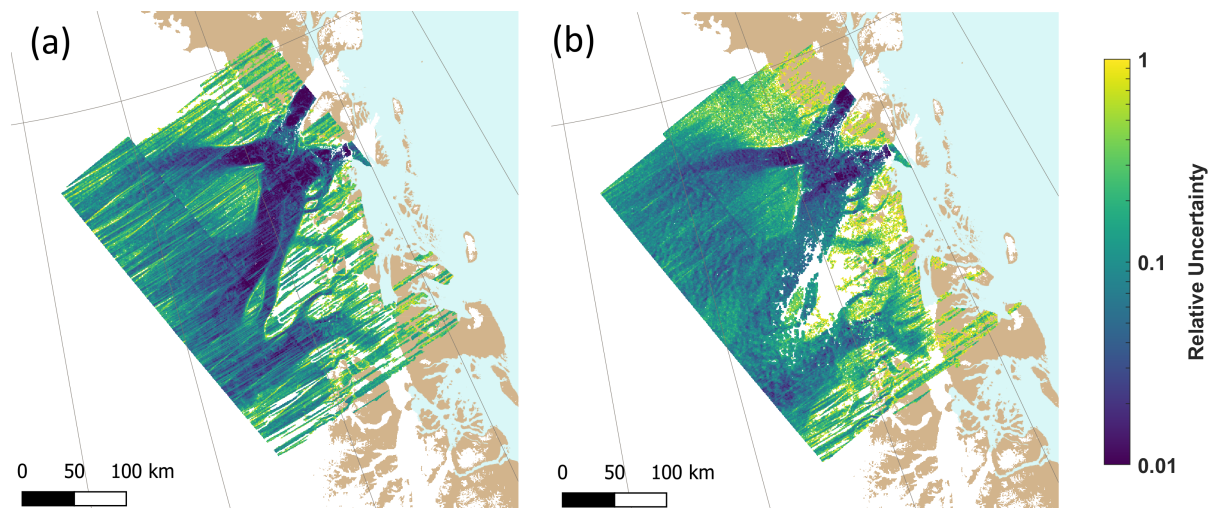
**Figure 8.** Relative horizontal velocity error estimates for the single-pair velocity maps in 7, (a) 6-day Pair acquired 2016-10-11 and 2016-10-17, (b) 12-day Pair acquired 2016-10-11 and 2016-10-23.

## 6 Properties of the Promice Ice Velocity Product

The PROMICE ice velocity product is designed as a compromise between good spatial coverage, high temporal resolution, and low noise. Other combinations of 6 day and 12 day pairs are possible resulting in different a temporal resolution and spatial coverage. We explore other possibilities for products and compare them to the PROMICE ice velocity product with respect to coverage and noise. These products are time series of mosaics consisting of (see Table 4):

1. All 6 day pairs (no 12 day pairs) within 2 Sentinel-1A cycles (**6dOnly**).

2. All 12 day pairs (no 6 day pairs) within 2 Sentinel-1A cycles (**12dOnly**).

3. All 6 day pairs (no 12 day pairs) within 1 Sentinel-1A cycle (**6dOnly_1cycle**).

Time series number 3 **6dOnly_1cycle** thus has twice the frequency compared to the PROMICE product.

Data coverage for each mosaic in each time series is displayed in the top panel of Fig. 9. We defined the coverage as the fraction of grid points that contains data on the ice sheet in a given mosaic. We have included a time series in the analysis called **All-pairsNoCull**, which includes the same data as the PROMICE product, but has not undergone the culling procedure described in Subsection 4.5. If all grid points on the ice sheet contains data then coverage is 1. All timeseries have close to full coverage during peak winter, where a campaign ensures full IW coverage of the ice sheet over a number of cycles. The coverage of the PROMICE product drops to $\sim 0.7$ outside the campaigns with a low during summer months. The lower panel of Fig. 9 shows the mean of the reported standard deviation for each map in the time series. In general, when coverage is low the noise goes up and vice versa. The 6dOnly_1cycle is the timeseries with highest reported noise level.

**Table 4.** Info on timeseries of mosaics from Sentinel-1 data. All-pairsNoCull contains the same data as the PROMICE product, but has not undergone the culling procedure described in Section 4.5.

|  | Temporal resolution | All 12d pairs included | All 6d pairs included |
|---|---|---|---|
| PROMICE Product (All-pairs) | 24d | x | x |
| 6dOnly | 24d |  | x |
| 12dOnly | 24d | x |  |
| 6dOnly_1cycle | 12d |  | x |
| All-pairsNoCull | 24d | x | x |

Figure 10 provides a spatial view of the fraction of all mosaics that have data in each grid point for each of the time series. Blue colors indicate that a grid point rarely has data, while yellow indicates a temporal coverage close to $100\%$. All four time series have a large blue area in the ice sheet interior, where SAR data in IW mode is rarely acquired as is evident from Fig. 2. The same explanation is true for the smaller triangular areas in the Melville Bay area and northern Greenland as well as

5 the Scoresbysund area. However, the large blue/green area along the southeast ice sheet margin as well as an area in southern Greenland, one north of Rink Glacier in West Greenland, and one in the Melville Bay area all have routine SAR IW acquisitions every 6 days. This will be discussed in the following.

The coverage and quality of each mosaic depend both on the SAR data coverage, the amount of data going into each mosaic as well as on how the properties of the ice-sheet surface have changed between acquisitions (Section 5, Section 4.4 and Fig. 2a).

10 The PROMICE product has the best coverage of the time series in Table 4 (excluding All-pairsNoCull) (Fig. 9 and 10) as it includes all the pairs contained in both 12dOnly and 6dOnly. Figure 9 shows that most often the 6dOnly has better coverage than the 12dOnly and for some extended periods of time, it is comparable to the PROMICE product. However, both 12dOnly and 6dOnly timeseries have periods with significant drops in coverage, while the PROMICE product still performs well. The difference in coverage is caused by differences in data acquisition and ice-sheet surface-properties.

15 Not all tracks have both 12 day and 6 day coverage and often tracks in the interior are only covered by 12d pairs. This is revealed by the lighter blue to green coloring of the interior for 12dOnly compared to the dark blue for 6dOnly in Fig. 10. 6dOnly has better coverage along the ice sheet margins compared to 12dOnly, because coherence is more likely to be preserved for shorter temporal baselines as discussed earlier in 3.1. The PROMICE product mosaics thus have better coverage than both 6dOnly and 12dOnly, because they each have coverage where the other does not. However, even using the short 6 day temporal

20 baseline some areas consistently have low coherence and therefore rarely have ice velocity coverage. The largest of these areas is the Southeast ice sheet margin while the smaller areas include an area in southern Greenland, one north of Rink Glacier in West Greenland, and one in the Melville Bay area (Fig. 10). The areas are apparent in all time series, but are most pronounced in the 12dOnly series as a longer temporal baseline increases the probability of changes to the surface properties due to precipitation and/or surface melt. The areas discussed here largely coincide with the regions identified as high accumulation

25 percolation areas (HAPA) by Vandecrux et al. (2019) studying firn properties. HAPAs are areas on the ice sheet characterized
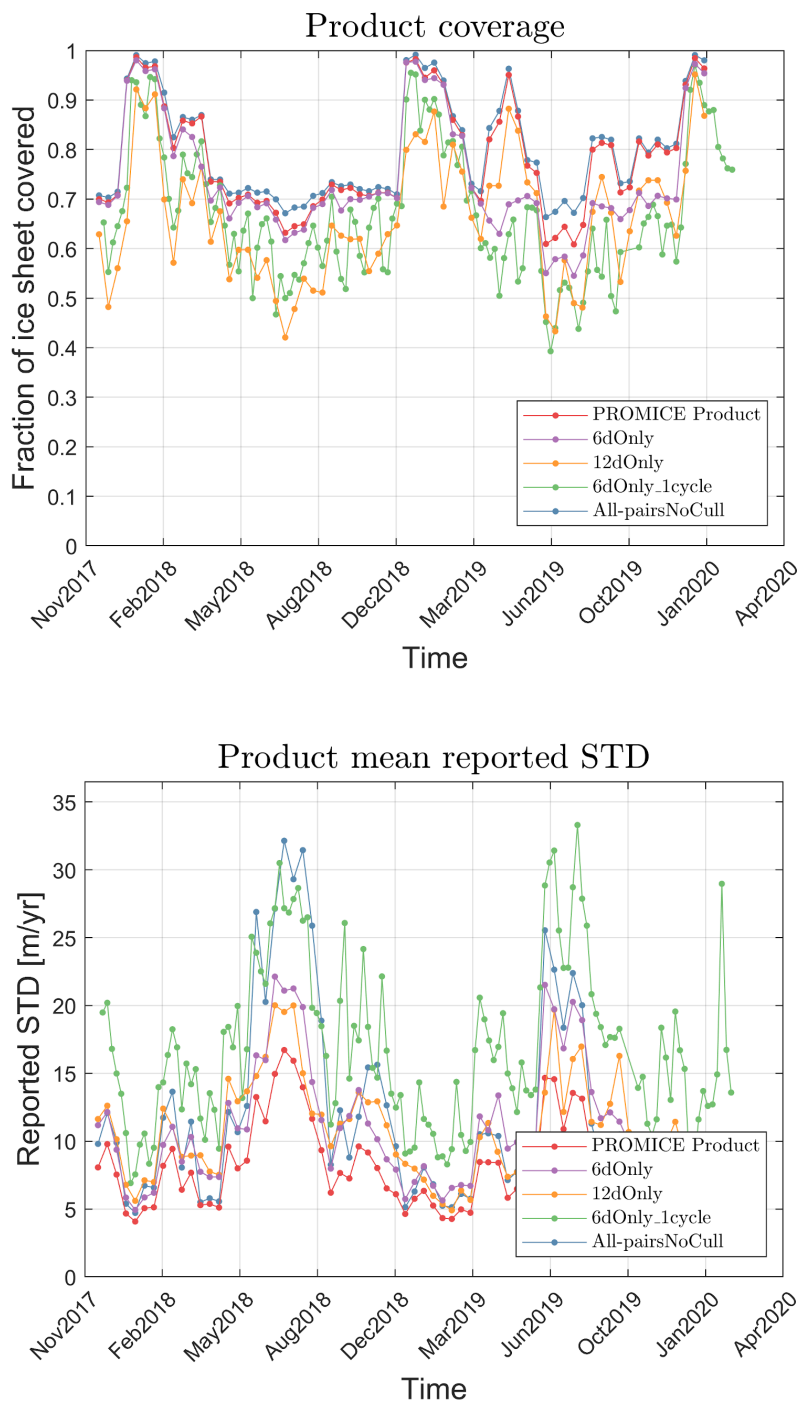
**Figure 9.** Coverage and reported mean standard deviation. The PROMICE ice velocity product (All -2 cycles) is shown in red.
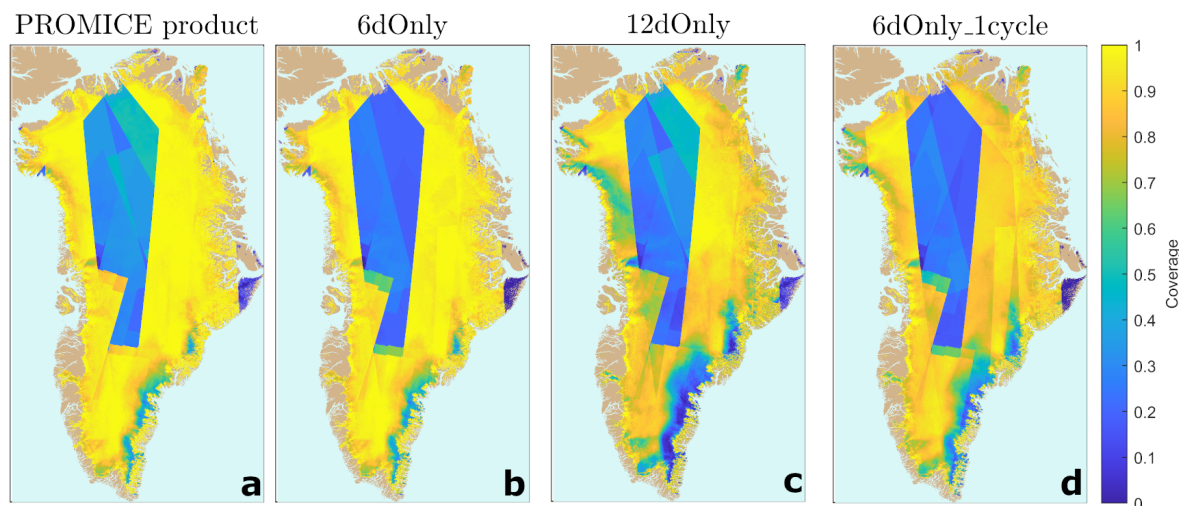
**Figure 10.** Effect of including 6 and 12 day pairs on coverage in the mosaic: a) The PROMICE ice velocity product b) 6dOnly time series c) 12dOnly timeseries and d) 6dOnly_1cycle timeseries.

by frequent precipitation events and surface melt-water that percolates into the firn -both processes changing the properties observed by the radar.

Figure 9 also shows the effect of performing the culling described in Subsection 4.5 on the time series as a whole. The All-pairsNoCull is the PROMICE Product without culling. Figure 9a shows that the effect on the coverage is minor, however

5 Fig. 9b shows that the average noise level is significantly reduced. The points that are culled are thus also the points that the IPP processor assigns a high uncertainty to.

In the PROMICE ice velocity product each mosaic includes all possible 6 and 12 day pairs within two consecutive Sentinel-1A cycles and the timestamps supplied with the product lists the timespan of the product (first and last date) as well as the midpoint time as specified in Table 1. This information is true for the mosaic, but not for a given grid point. This is due to:

10     – The SAR data (Fig. 2) is not acquired simultaneously over the GrIS as described in Subsection 3.1.

    – Different areas on the ice sheet are covered by a varying number of tracks/varying amount of data acquired at different times (also Fig. 2).

    – Although data is acquired, the processor is unable to detect displacement for some pixels or larger areas due to loss of coherence or the processing of an image pair fails for various reasons and is therefore not included in the final mosaic.

15 Another point to keep in mind is that the mosaic is a weighted average of the processed pairs spanning 24 days. This means that although the product has a high temporal resolution, the time series will be smoothed and likely miss short lived (real) peaks in velocity for instance during summer.

## 7 Validation

We validate the PROMICE ice velocity product against in-situ GPS measurements. Only a limited number of GPS measurements are available since the data should overlap in time with the period of the PROMICE ice velocity product and have a a temporal resolution comparable to or higher than the PROMICE ice velocity product. Furthermore, the measurements are
5 biased toward the slow moving parts of the ice sheet ablation zone. We compare the PROMICE ice velocity product to in-situ GPS data from the PROMICE automatic weather stations (AWS) (van As et al., 2011). Locations are displayed in Fig. 11.

PROMICE AWS measure a range of surface mass-balance components in the ablation zone of the Greenland Ice Sheet. The stations are per design located in slow moving areas with an average flow generally lower than 100 m/yr (Fig. 11). The position of the AWS is measured every hour using a single frequency GPS receiver and a small ceramic patch active antenna.
10 We use the freely available hourly positions ((Fausto and van As, 2019)) to calculate velocities using a workflow similar to that described in GIScci-Consortium (2018): Daily positions of the GPS stations are calculated as a mean of the hourly positions for each day. The velocity components are estimated using a weighted linear regression for each of the 24-day time spans of the velocity mosaics using the daily positions. The weights are inversely proportional to the number of hourly measurements going into the estimate of a daily position in order to account for gaps in the data.

15 Scatter plots of the satellite derived PROMICE ice velocity product (magnitude, $v_x$ and $v_y$ components) vs. PROMICE GPS derived ice velocities are displayed in Fig. 12. The standard deviation of the difference between the GPS measurements and the satellite derived velocity (from here on referred to as the standard deviation) is calculated along with the mean difference (bias) between GPS and satellite velocity (see first line in Table 5). These values reflect not only the uncertainty of the satellite product but also that of the GPS derived velocity. The expected error of the satellite product is estimated to be 10-30 m/yr for
20 individual pairs (GIScci-Consortium, 2013). The PROMICE product lies well within these bounds with a standard deviation and bias of 20 m/yr and -3 m/yr for the $v_x$ component and 27 m/yr and -2 m/yr for the $v_y$ component, respectively. The larger standard deviation for the $v_y$ component is expected: Due to the general North-South orientation of the satellite tracks (Fig. 2), the $v_y$ component is aligned roughly parallel to the azimuth direction (satellite flight path), and Sentinel-1 IW SLC images (see Section 3.1) have a much lower resolution in azimuth than in the range (line-of-)sight direction). We note that due to the
25 East/West orientation of most Greenland glaciers the range of the y-component in our validation is notably smaller than that of the x-component.

Hvidberg et al. (2020) carried out a validation of many available satellite-derived ice-velocity products using an array of 63 GPS stations around EGRIP camp ($75°38'$ N, $35°60'$ W) located on the Northeast Greenland Ice Stream. EGRIP camp is located in the ice-sheet accumulation zone and Hvidberg et al. (2020) measured an average speed in the central flow line of
30 55 m/yr. The ice thus flows slowly at this location. The PROMICE ice velocity product was included in this analysis, and they found an average standard deviation of 6.6 m/yr for the products within the period September 13, 2016 to August 8, 2019. This is a significantly lower value of the standard deviation compared to what the validation against the PROMICE GPS observations shows, but similar to the analysis carried out on stable ground in Subsection 5.2 (see Fig. 6). This difference is mainly due to two things: 1) In the accumulation zone, changes at the ice sheet surface are mainly due to snow fall and redistribution by wind.

In contrast, in the ablation zone, where all the PROMICE GPS stations are located, the surface properties are influenced by several factors e.g. melt, high accumulation rates, and rain. This influences the coherence of image pairs and thereby increases uncertainty in the velocity product in these areas. 2) The uncertainty of the GPS measurements reported in Hvidberg et al. (2020) is lower compared to the PROMICE GPS observations. This is due to both the longer temporal baseline between

5   measurements as well as the data acquisition time of 2-4 hours per data point. The velocities derived from the PROMICE GPS observations may therefore carry a non negligible part of the uncertainty in the validation. None of the other products in the comparison by Hvidberg et al. (2020) have a similar high temporal resolution as the PROMICE ice velocity product. However, a 3-year average of the PROMICE ice velocity product was also included in the analysis and Hvidberg et al. (2020) found that it had a standard deviation (0.7 m/yr) similar to other offset/feature tracking products covering longer timespans like the annual

10  maps from ESA CCI (Greenland Ice Sheet velocity maps from Sentinel-1 (Nagler et al., 2015)) and MEaSUREs Greenland Annual Ice Sheet Velocity Mosaics from SAR and Landsat, Version 1 [2015-2018] (Joughin et al., 2010), which have average values of 1.5 and 1.4 m/yr, respectively (Hvidberg et al., 2020) Supp. The standard deviation of the 3-year average of the PROMICE product is lower than for the annual maps, most likely because it includes more data. This is also a conclusion drawn by Hvidberg et al. (2020).

15  The 12dOnly and 6dOnly time series introduced in Section 6 have similar standard deviations as the PROMICE product, when compared to the velocity derived from the PROMICE GPSs, whereas the higher temporal resolution product, 6dOnly_1cycle, has a significantly higher standard deviation. The PROMICE ice velocity product has the lowest standard deviation of the four. Using only 6 day pairs it is also possible to define a Greenland-wide product with a temporal resolution of 12 days, -the 6dOnly_1cycle product. It has the clear advantage of resolving the dynamics of the outlet glaciers even better,

20  although this comes with the price of increased noise due to both the shorter temporal baseline and the geolocation bias as well as reduced coverage of each mosaic (Fig. 9a and b, Fig. 10 and Table 5). It worth noticing that the outer most parts of the outlet glaciers still have reasonable coverage and for studying changes in fast flow in these areas the increased temporal resolution may outweigh the downsides. The PROMICE ice velocity product as defined here provides a reasonable compromise between high coverage, temporal resolution, and noise.

25  The uncertainty reported in the ice velocity product is lower than the values we found during our validation. The average standard deviation found in Hvidberg et al. (2020) is more comparable. The origin of some errors is such that the algorithm is unable to account for them. This is especially true for the spatially correlated errors caused by ionospheric scintillations (Section 5.4), which are not fully estimated by the error estimation algorithm (Section 5.5). A second issue is the distribution of the PROMICE AWSs biased towards the slow flowing parts of the ablation zone as well as the uncertainly on the velocity

30  estimates from these data.

For a time series of mosaics like the PROMICE ice velocity product, errors will vary both spatially and temporally due to the sources described in Section 5 as well as to variations in data coverage (Subsection 4.4 and Fig. 2a). A spatially better distributed set of validation data, which is not biased towards slow flowing areas in the ablation zone would help assess whether the reported product errors capture this correctly. The analysis above, however, shows that the size of the product errors are as

35  expected.
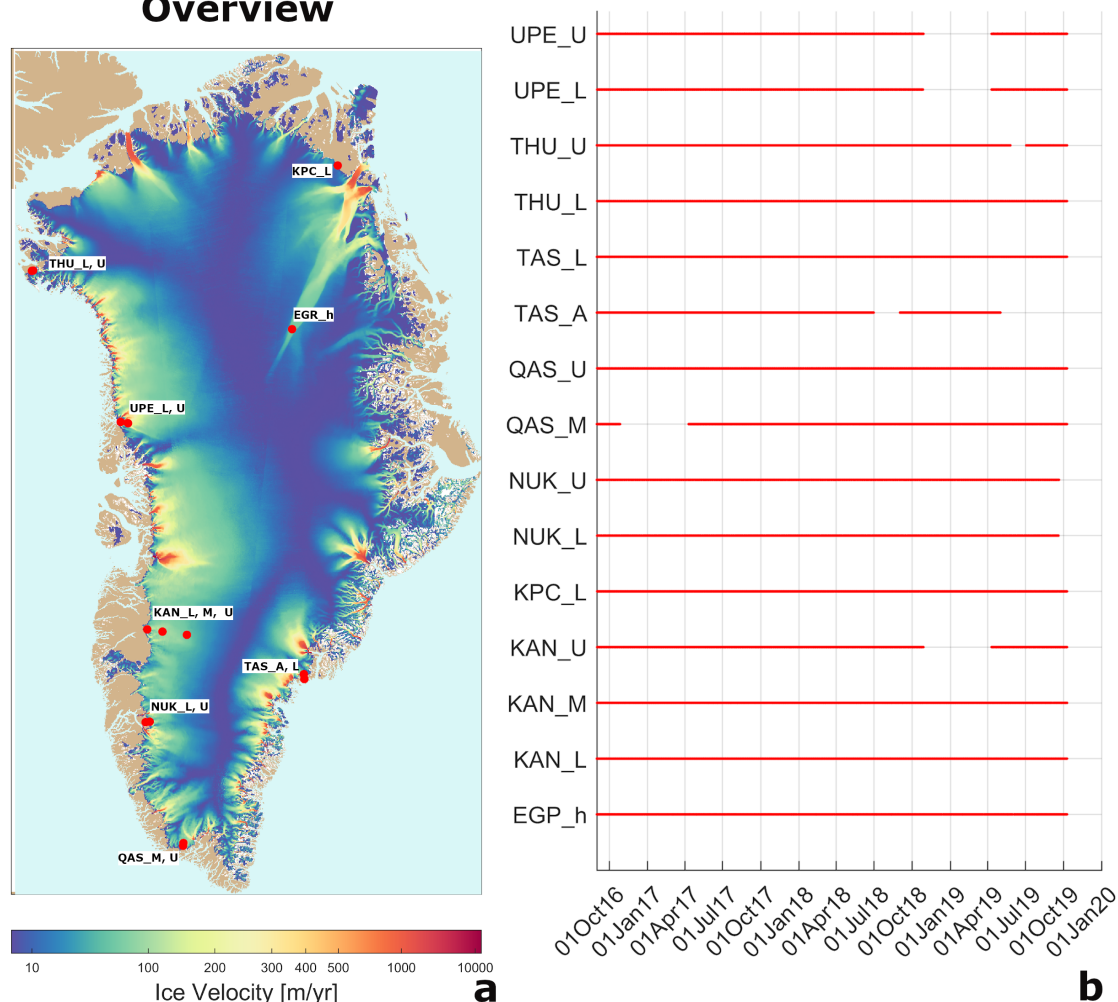
**Figure 11.** Overview of PROMICE GPS data: a) Locations of the PROMICE GPS stations on the Greenland Ice Sheet. The ice velocity mosaic used as base layer is a 3 year average of all the PROMICE ice velocity maps spanning September 2016 to September 2019. b) List of PROMICE GPS stations used in the validation and their data coverage.

## 8   Living Data: Updates and Improvements

PROMICE will continue to distribute and update the PROMICE Ice Velocity product based on the Sentinel-1 data collected and released by ESA and the Copernicus programme. We aim to deliver a clean and homogenous data product and offer the possibility of user-interaction and addressing issues with the data product. Associated with PROMICE, we have a

5   user-contributable dynamic web-based data archive (GitHub), which list known data quality issues [https://github.com/GEUS-
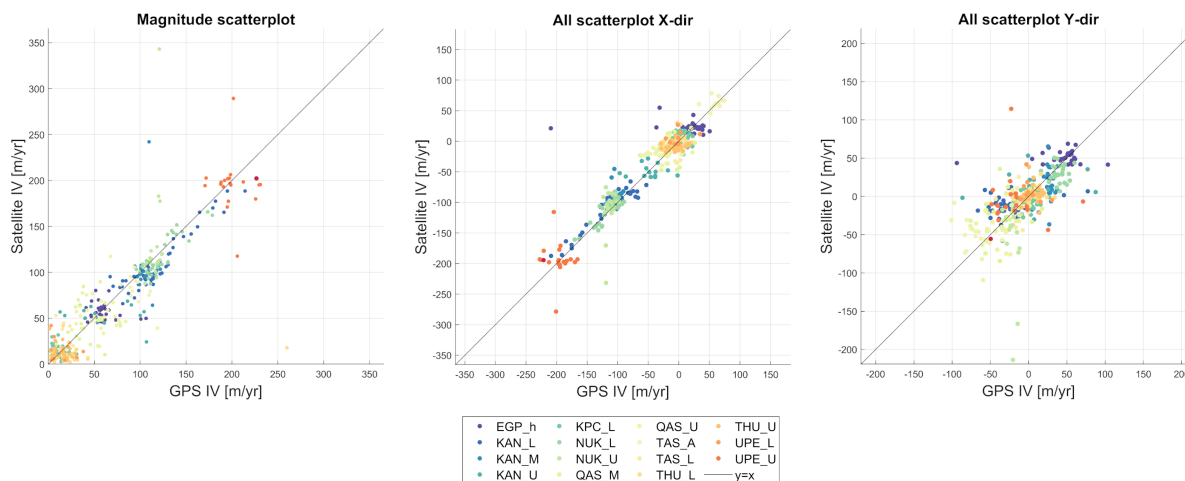
**Figure 12.** Scatterplots of PROMICE GPS IV vs PROMICE ice velocity.

**Table 5.** Statistics of the validation of the satellite IV products using GPS data.

| Product | Magnitude | | x-dir | | y-dir | |
|---|---|---|---|---|---|---|
| | Std | Bias | Std | Bias | Std | Bias |
| | [m/yr] | [m/yr] | [m/yr] | [m/yr] | [m/yr] | [m/yr] |
| PROMICE Product (All pairs) | 19 | 4 | 20 | -3 | 27 | -2 |
| 6dOnly | 22 | 0 | 21 | -2 | 31 | -1 |
| 12dOnly | 19 | 4 | 20 | -2 | 28 | 0 |
| 6dOnly_1cycle | 34 | 9 | 31 | -3 | 40 | -2 |

PROMICE/Sentinel-1_Greenland_Ice_Velocity]. On the GitHub page, we also offer the opportunity for data users to add and document new issues. Documenting dataset issues is often simpler than correcting them and future dataset versions will implement fixes to any verified issues as soon as they are done. All fixed issues will be tagged as closed and remain visible for new users.

5    We encourage users who are working with Sentinel-1 and the PROMICE ice-velocity data to search the issue database and see if there are any known data issues relevant to their needs. We find it likely that there are issues unknown to us in the existing data and new issues may be found in the future data collection pipeline. We will do our best to improve the dataset with user-based help through the GitHub page.

## 9 Summary and Outlook

We have presented the PROMICE ice velocity product -a time series of GrIS wide velocity mosaics (September 2016 to present) based on Sentinel-1 SAR data. The product has a 500 m spatial- and 24 day temporal resolution and is produced in an operational setup using the IPP processor. A new mosaic is produced every 12 days and is made available within 10 days of the last included acquisition. During the winter campaigns, this lag is larger due to the amount of data to be processed. Validation against PROMICE AWS GPS data show that the standard deviation of the difference between the ice velocity product and the GPS data is 20 m/yr and 27 m/yr for $v_x$ and $v_y$-component, respectively. This is within the expected uncertainty range of 10-30 m/yr (GIScci-Consortium, 2013). However, we expect the actual values pertaining to the PROMICE ice velocity product to be lower as the PROMICE AWS GPS data carry a non negligible part of the uncertainty. This is also indicated by the study of Hvidberg et al. (2020). Better spatially distributed validation data with low uncertainty would help assessing whether the processor captures the spatially and temporally varying uncertainty field correctly.

Ice velocities are retrieved by applying intensity offset-tracking to Sentinel-1 images acquired 6 and 12 days apart. The resulting velocity maps from all image pairs acquired during a 24-day period are temporally averaged and mosaicked to produce a consistent coverage. The processing chain is described in detail from the input data to the final outlier removal. We discuss the various error sources, which include biases and smoothly varying errors due to orbit and timing errors, noise-like errors due to changes in radar backscatter between radar acquisitions, and errors due to ionospheric scintillations. The error estimation approach is also described.

We show how the product coverage vary temporally and spatially in response to variations in SAR data acquisitions and seasonal changes in surface properties. The Southeast GrIS margin has good Sentinel-1 SAR data coverage, but often has gaps in the mosaics due to changes in the surface properties caused by surface melt and high precipitation rates. Other areas, like the small triangular area in the Melville Bay area, have low coverage in the mosaics simply due to lack of SAR data.

The PROMICE Ice Velocity product will continue to update as long as the Sentinel-1 satellites are in operation. We will continue to make improvements to the product, and these updates will be posted at https://github.com/GEUS-PROMICE/Sentinel-1_Greenland_Ice_Velocity. Users are encouraged to add and document product issues or suggest improvements.

The PROMICE ice velocity product presented was originally intended primarily to calculate ice discharge through marine-terminating glaciers of the GrIS as done in Mankoff et al. (2020). The PROMICE ice velocity product is thus less suited for studying very short-lived changes in the velocity structure, as observed in-situ by e.g. Bartholomew et al. (2012) and Ahlstrøm et al. (2013) or through higher frequency acquisitions/non-mosaic products of satellite imagery as done by e.g. Sundal et al. (2013) and Davison et al. (2020). By not mosaicking all the individual image pairs like we do for the PROMICE ice velocity product, a much higher temporal resolution over a limited region is possible. Yet, the spatially comprehensive and temporally consistent nature of the PROMICE ice velocity product makes it attractive also for longer term large-scale monitoring of the GrIS velocity structure and glacier dynamics as done by Vijay et al. (2019) and Solgaard et al. (2020).

## 10  Data availability

The PROMICE Ice Velocity product has DOI: https://doi.org/10.22008/promice/data/sentinel1icevelocity/greenlandicesheet
and is available at https://dataverse01.geus.dk/dataverse/Ice_velocity. The product is updated regularly with a new mosaic
every 12 days. Check out https://github.com/GEUS-PROMICE/Sentinel-1_Greenland_Ice_Velocity for updates and for posting
5  issues.

*Author contributions.*  AS and AK designed and produced the PROMICE ice velocity product. AK, JPMB and JD developed the processing
software. RSF and KDM set up the data-curation framework. AS and AK prepared the manuscript with contributions from all co-authors.

*Competing interests.*  Authors declare that they have no conflict of interest.

*Acknowledgements.*  Ice velocity maps were produced as part of the Programme for Monitoring of the Greenland Ice Sheet (PROMICE) using
10  Copernicus Sentinel-1 SAR images distributed by ESA, and were provided by the Geological Survey of Denmark and Greenland (GEUS) at
http://www.promice.dk. AWS data from the Programme for Monitoring of the Greenland Ice Sheet (PROMICE) and the Greenland Analogue
Project (GAP) were provided by the Geological Survey of Denmark and Greenland (GEUS) at http://www.promice.dk.

# References

Ahlstrøm, A. P., Andersen, S. B., Andersen, M. L., Machguth, H., Nick, F. M., Joughin, I., Reijmer, C. H., van de Wal, R. S. W., Merryman Boncori, J. P., Box, J. E., Citterio, M., van As, D., Fausto, R. S., and Hubbard, A.: Seasonal velocities of eight major marine-terminating outlet glaciers of the Greenland ice sheet from continuous in situ GPS instruments, Earth System Science Data, 5, 277–287, https://doi.org/10.5194/essd-5-277-2013, 2013.

Bartholomew, I., Nienow, P., Sole, A., Mair, D., Cowton, T., and King, M. A.: Short-term variability in Greenland Ice Sheet motion forced by time-varying meltwater drainage: Implications for the relationship between subglacial drainage system behavior and ice velocity, Journal of Geophysical Research: Earth Surface, 117, https://doi.org/https://doi.org/10.1029/2011JF002220, 2012.

Boncori, J. P. M., Andersen, M. L., Dall, J., Kusk, A., Kamstra, M., Andersen, S. B., Bechor, N., Bevan, S., Bignami, C., Gourmelen, N., and et al.: Intercomparison and Validation of SAR-Based Ice Velocity Measurement Techniques within the Greenland Ice Sheet CCI Project, Remote Sensing, 10, 929, https://doi.org/10.3390/rs10060929, http://dx.doi.org/10.3390/rs10060929, 2018.

Davison, B. J., Sole, A. J., Cowton, T. R., Lea, J. M., Slater, D. A., Fahrner, D., and Nienow, P. W.: Subglacial Drainage Evolution Modulates Seasonal Ice Flow Variability of Three Tidewater Glaciers in Southwest Greenland, Journal of Geophysical Research: Earth Surface, 125, e2019JF005 492, https://doi.org/https://doi.org/10.1029/2019JF005492, 2020.

de Lange, R., Luckman, A., and Murray, T.: Improvement of Satellite Radar Feature Tracking for Ice Velocity Derivation by Spatial Frequency Filtering, IEEE Transactions on Geoscience and Remote Sensing, 45, 2309–2318, https://doi.org/10.1109/TGRS.2007.896615, 2007.

De Zan, F.: Accuracy of Incoherent Speckle Tracking for Circular Gaussian Signals, IEEE Geoscience and Remote Sensing Letters, 11, 264–267, https://doi.org/10.1109/LGRS.2013.2255259, 2014.

De Zan, F. and Guarnieri, A. M.: TOPSAR: Terrain observation by progressive scans, IEEE Transactions on Geoscience and Remote Sensing, https://doi.org/10.1109/TGRS.2006.873853, 2006.

Fausto, R. and van As, D.: Programme for monitoring of the Greenland ice sheet (PROMICE): Automatic weather station data. Version: v03, Geological survey of Denmark and Greenland (GEUS)., https://doi.org/DOI: https://doi.org/10.22008/promice/data/aws, 2019.

Gardner, A. S., Fahnestock, M. A., and Scambos, T. A.: ITS_LIVE Regional Glacier and Ice Sheet Surface Velocities., Data archived at National Snow and Ice Data Center, https://doi.org/10.5067/6II6VW8LLWJ7, 2019.

GIScci-Consortium: Comprehensive Error Characterisation Report for the Greenland Ice Sheet cci project of ESA's Climate Change Initiative, version 1.2, Tech. rep., European Space Agency, 2013.

GIScci-Consortium: Product Validation and Intercomparison Report (PVIR) for the Greenland Ice Sheet cci project of ESA's Climate Change Initiative, version 3.0, Tech. rep., European Space Agency, 2018.

Gisinger, C., Schubert, A., Breit, H., Garthwaite, M., Balss, U., Willberg, M., Small, D., Eineder, M., and Miranda, N.: In-Depth Verification of Sentinel-1 and TerraSAR-X Geolocation Accuracy Using the Australian Corner Reflector Array, IEEE Transactions on Geoscience and Remote Sensing, pp. 1–28, https://doi.org/10.1109/TGRS.2019.2961248, 2020.

Gomba, G.: Estimation of ionosphere-compensated azimuth ground motion with sentinel-1, Proceedings of the European Conference on Synthetic Aperture Radar, Eusar, pp. 87–90, 2018.

Gray, A., Mattar, K., Vachon, P., Bindschadler, R., Jezek, K., Forster, R., and Crawford, J.: InSAR results from the RADARSAT Antarctic Mapping Mission data: estimation of glacier motion using a simple registration procedure, in: IGARSS '98. Sensing and Managing the

Environment. 1998 IEEE International Geoscience and Remote Sensing. Symposium Proceedings. (Cat. No.98CH36174), pp. 1638–1640 vol.3, IEEE, https://doi.org/10.1109/IGARSS.1998.691662, http://ieeexplore.ieee.org/document/691662/, 1998.

Gray, A. L., Mattar, K. E., and Sofko, G.: Influence of Ionospheric Electron Density Fluctuations on Satellite Radar Interferometry, Geophysical Research Letters, https://doi.org/10.1029/2000GL000016, 2000.

5   Howat, I. M., Box, J. E., Ahn, Y., Herrington, A., and McFadden, E. M.: Seasonal variability in the dynamics of marine-terminating outlet glaciers in Greenland, Journal of Glaciology, 56, 601–613, https://doi.org/10.3189/002214310793146232, 2010.

Howat, I. M., Negrete, A., and Smith, B. E.: The Greenland Ice Mapping Project (GIMP) land classification and surface elevation data sets, The Cryosphere, 8, 1509–1518, https://doi.org/10.5194/tc-8-1509-2014, https://tc.copernicus.org/articles/8/1509/2014/, 2014.

Hvidberg, C. S., Grinsted, A., Dahl-Jensen, D., Khan, S. A., Kusk, A., Andersen, J. K., Neckel, N., Solgaard, A., Karlsson, N. B., Kjær,

10  H. A., and Vallelonga, P.: Surface velocity of the Northeast Greenland Ice Stream (NEGIS): assessment of interior velocities derived from satellite data by GPS, The Cryosphere, 14, 3487–3502, https://doi.org/10.5194/tc-14-3487-2020, 2020.

Joughin, I.: MEaSUREs Greenland Annual Ice Sheet Velocity Mosaics from SAR and Landsat, Version 2., Boulder, Colorado USA. NASA National Snow and Ice Data Center Distributed Active Archive Center., https://doi.org/10.5067/TZZDYD94IMJB, 2020a.

Joughin, I.: MEaSUREs Greenland Monthly Ice Sheet Velocity Mosaics from SAR and Landsat, Version 2., Boulder, Colorado USA. NASA

15  National Snow and Ice Data Center Distributed Active Archive Center., https://doi.org/0.5067/11MJZGPBK3ZF, 2020b.

Joughin, I.: MEaSUREs Greenland Quarterly Ice Sheet Velocity Mosaics from SAR and Landsat, Version 2, Boulder, Colorado USA. NASA National Snow and Ice Data Center Distributed Active Archive Center., https://doi.org/10.5067/3ZMCUIFDYJG4, 2020c.

Joughin, I., Smith, B. E., Howat, I. M., Scambos, T., and Moon, T.: Greenland flow variability from ice-sheet-wide velocity mapping, Journal of Glaciology, 56, 415–430, https://doi.org/10.3189/002214310792447734, 2010.

20  Joughin, I., Smith, B. E., and Howat, I.: Greenland Ice Mapping Project: ice flow velocity variation at sub-monthly to decadal timescales, The Cryosphere, 12, 2211–2227, https://doi.org/10.5194/tc-12-2211-2018, 2018.

Joughin, L. R., Kwok, R., and Fahnestock, M. A.: Interferometric estimation of three-dimensional ice-flow using ascending and descending passes, IEEE Transactions on Geoscience and Remote Sensing, https://doi.org/10.1109/36.655315, 1998.

Kusk, A., Boncori, J., and Dall, J.: An automated system for ice velocity measurement from SAR, in: Proceedings of the 12th European

25  Conference on Synthetic Aperture Radar (EUSAR 2018), Proceedings of the European Conference on Synthetic Aperture Radar, pp. 929–932, VDE Verlag, 2018.

Liao, H., Meyer, F. J., Scheuchl, B., Mouginot, J., Joughin, I., and Rignot, E.: Ionospheric correction of InSAR data for accurate ice velocity measurement at polar regions, Remote Sensing of Environment, 209, 166 – 180, https://doi.org/https://doi.org/10.1016/j.rse.2018.02.048, http://www.sciencedirect.com/science/article/pii/S0034425718300580, 2018.

30  Mankoff, K. D., Solgaard, A., Colgan, W., Ahlström, A. P., Khan, S. A., and Fausto, R. S.: Greenland Ice Sheet solid ice discharge from 1986 through March 2020, Earth System Science Data, 12, 1367–1383, https://doi.org/10.5194/essd-12-1367-2020, 2020.

Mattar, K. E. and Gray, A. L.: Reducing ionospheric electron density errors in satellite radar interferometry applications, Canadian Journal of Remote Sensing, 28, 593–600, https://doi.org/10.5589/m02-051, 2002.

Miranda, N.: Definition of the TOPS SLC deramping function for products generated by the S-1 IPF (Technical Note COPE-GSEG-EOPG-

35  TN-14-0025, Issue 1, Rev. 3), Tech. rep., European Space Agency, 2017.

Moon, T., Joughin, I., Smith, B., van den Broeke, M. R., van de Berg, W. J., Noël, B., and Usher, M.: Distinct patterns of seasonal Greenland glacier velocity, Geophysical Research Letters, 41, 7209–7216, https://doi.org/https://doi.org/10.1002/2014GL061836, 2014.

Moon, T. A., Gardner, A. S., Csatho, B., Parmuzin, I., and Fahnestock, M. A.: Rapid Reconfiguration of the Greenland Ice Sheet Coastal Margin, Journal of Geophysical Research: Earth Surface, 125, e2020JF005 585, https://doi.org/https://doi.org/10.1029/2020JF005585, 2020.

Mouginot, J., Bjørk, A. A., Millan, R., Scheuchl, B., and Rignot, E.: Insights on the Surge Behavior of Storstrøm-men and L. Bistrup Bræ, Northeast Greenland, Over the Last Century, Geophysical Research Letters, 45, 11,197–11,205, https://doi.org/https://doi.org/10.1029/2018GL079052, 2018.

Mouginot, J., Rignot, E., Millan, R., and Wood, M.: Annual Ice Velocity of the Greenland Ice Sheet (1972-1990), Dryad, Dataset., https://doi.org/10.7280/D1MM37, 2019a.

Mouginot, J., Rignot, E., Scheuchl, B., Millan, R., and Wood, M. .: Annual Ice Velocity of the Greenland Ice Sheet (1991-2000), Dryad, Dataset., https://doi.org/10.7280/D1GW91, 2019b.

Mouginot, J., Rignot, E., Scheuchl, B., Wood, M., and Millan, R.: Annual Ice Velocity of the Greenland Ice Sheet (2001-2010), Dryad, Dataset., https://doi.org/10.7280/D1595V, 2019c.

Mouginot, J., Rignot, E., Scheuchl, B., Wood, M., and Millan, R.: Annual Ice Velocity of the Greenland Ice Sheet (2010-2017), Dryad, Dataset., https://doi.org/10.7280/D11H3X, 2019d.

Nagler, T., Rott, H., Hetzenecker, M., Wuite, J., and Potin, P.: The Sentinel-1 mission: New opportunities for ice sheet observations, Remote Sensing, https://doi.org/10.3390/rs70709371, 2015.

Peter, H., Jäggi, A., Fernández, J., Escobar, D., Ayuga, F., Arnold, D., Wermuth, M., Hackel, S., Otten, M., Simons, W., Visser, P., Hugen-tobler, U., and Féménias, P.: Sentinel-1A – First precise orbit determination results, Advances in Space Research, 60, 879 – 892, https://doi.org/https://doi.org/10.1016/j.asr.2017.05.034, http://www.sciencedirect.com/science/article/pii/S0273117717303794, 2017.

Rignot, E. and Kanagaratnam, P.: Changes in the Velocity Structure of the Greenland Ice Sheet, Science, 311, 986–990, https://doi.org/10.1126/science.1121381, 2006.

Rosenau, R., Scheinert, M., and Dietrich, R.: A processing system to monitor Greenland outlet glacier velocity varia-tions at decadal and seasonal time scales utilizing the Landsat imagery, Remote Sensing of Environment, 169, 1 – 19, https://doi.org/https://doi.org/10.1016/j.rse.2015.07.012, 2015.

Schubert, A., Miranda, N., Geudtner, D., and Small, D.: Sentinel-1A/B combined product geolocation accuracy, Remote Sensing, 9, 607, https://doi.org/10.3390/rs9060607, 2017.

Shepherd, A., Ivins, E., Rignot, E., Smith, B., van den Broeke, M., Velicogna, I., Whitehouse, P., Briggs, K., Joughin, I., Krinner, G., Nowicki, S., Payne, T., Scambos, T., Schlegel, N., Geruo, A., Agosta, C., Ahlstrøm, A., Babonis, G., Barletta, V. R., Bjørk, A. A., Blazquez, A., Bonin, J., Colgan, W., Csatho, B., Cullather, R., Engdahl, M. E., Felikson, D., Fettweis, X., Forsberg, R., Hogg, A. E., Gallee, H., Gardner, A., Gilbert, L., Gourmelen, N., Groh, A., Gunter, B., Hanna, E., Harig, C., Helm, V., Horvath, A., Horwath, M., Khan, S., Kjeldsen, K. K., Konrad, H., Langen, P. L., Lecavalier, B., Loomis, B., Luthcke, S., McMillan, M., Melini, D., Mernild, S., Mohajerani, Y., Moore, P., Mottram, R., Mouginot, J., Moyano, G., Muir, A., Nagler, T., Nield, G., Nilsson, J., Noël, B., Otosaka, I., Pattle, M. E., Peltier, W. R., Pie, N., Rietbroek, R., Rott, H., Sørensen, L. S., Sasgen, I., Save, H., Scheuchl, B., Schrama, E., Schröder, L., Seo, K.-W., Simonsen, S. B., Slater, T., Spada, G., Sutterley, T., Talpe, M., Tarasov, L., Jan van de Berg, W., van der Wal, W., van Wessem, M., Vishwakarma, B. D., Wiese, D., Wilton, D., Wagner, T., Wouters, B., and Wuite, J.: Mass balance of the Greenland Ice Sheet from 1992 to 2018, Nature, 2019.

Solgaard, A. and Kusk, A.: Greenland Ice Velocity from Sentinel-1 Edition 2, https://doi.org/10.22008/promice/data/sentinel1icevelocity/greenlandicesheet, 2021.

Solgaard, A. M., Simonsen, S. B., Grinsted, A., Mottram, R., Karlsson, N. B., Hansen, K., Kusk, A., and Sørensen, L. S.: Hagen Bræ: A Surging Glacier in North Greenland—35 Years of Observations, Geophysical Research Letters, 47, e2019GL085 802, https://doi.org/https://doi.org/10.1029/2019GL085802, 2020.

Strozzi, T., Luckman, A., Murray, T., Wegmüller, U., and Werner, C. L.: Glacier motion estimation using SAR offset-tracking procedures, IEEE Transactions on Geoscience and Remote Sensing, https://doi.org/10.1109/TGRS.2002.805079, 2002.

Sundal, A., Shepherd, A., van den Broeke, M., Van Angelen, J., Gourmelen, N., and Park, J.: Controls on short-term variations in Greenland glacier dynamics, Journal of Glaciology, 59, 883–892, https://doi.org/10.3189/2013JoG13J019, 2013.

van As, D., Fausto, R. S., and PROMICE project team, .: Programme for Monitoring of the Greenland Ice Sheet (PROMICE): first temperature and ablation records, GEUS Bulletin, 23, 73–76, 2011.

Vandecrux, B., MacFerrin, M., Machguth, H., Colgan, W. T., van As, D., Heilig, A., Stevens, C. M., Charalampidis, C., Fausto, R. S., Morris, E. M., Mosley-Thompson, E., Koenig, L., Montgomery, L. N., Miège, C., Simonsen, S. B., Ingeman-Nielsen, T., and Box, J. E.: Firn data compilation reveals widespread decrease of firn air content in western Greenland, The Cryosphere, 13, 845–859, https://doi.org/10.5194/tc-13-845-2019, 2019.

Vijay, S., Khan, S. A., Kusk, A., Solgaard, A. M., Moon, T., and Bjørk, A. A.: Resolving Seasonal Ice Velocity of 45 Greenlandic Glaciers With Very High Temporal Details, Geophysical Research Letters, 46, 1485–1495, https://doi.org/https://doi.org/10.1029/2018GL081503, 2019.

Westerweel, J. and Scarano, F.: Universal outlier detection for PIV data, Experiments in Fluids, 39, 1096–1100, https://doi.org/10.1007/s00348-005-0016-6, 2005.